Combining Total Variation Regularization with Window-based Time Delay Estimation in Ultrasound Elastography

M. Mirzaei, A. Asif and H. Rivaz

***Abstract*—A major challenge of free-hand palpation ultrasound elastography (USE) is estimating displacement of RF samples between pre- and post-compressed RF data. The problem of displacement estimation is ill-posed since the displacement of one sample by itself cannot be uniquely calculated. To resolve this problem, two categories of methods have emerged. The first category assumes that the displacement of samples within a small window surrounding the reference sample is constant. The second class imposes smoothness regularization and optimizes an energy function. Herein, we propose a novel method that combines both approaches, and as such, is more robust to noise. The second contribution of this work is the introduction of the L1 norm as the regularization term in our cost function, which is often referred to as the total variation (TV) regularization. Compared to previous work that used the L2 norm regularization, optimization of the new cost function is more challenging. However, the advantages of using the L1 norm are twofold. First, it leads to substantial improvement in the sharpness of displacement estimates. Second, to optimize the cost function with the L1 norm regularization, we use an iterative method that further increases the robustness. We name our proposed method OVERWIND (tOtal Variation Regularization and WINDow-based time delay estimation) and show that it is robust to signal decorrelation and generates sharp displacement and strain maps for simulated, experimental phantom and *in-vivo* data. In particular, OVERWIND improves strain contrast to noise ratio (CNR) by 27.26%, 144.05% and 49.90% on average in simulation, phantom and *in-vivo* data, respectively, compared to our recent Global Ultrasound Elastography (GLUE) [1] method.**

***Index Terms*—Ultrasound elastography, Time delay estimation (TDE), Total variation regularization, Window-based TDE**

I. Introduction

Ultrasound imaging is one of the most commonly used imaging modalities since it is inexpensive, safe, convenient and widely available including at the bedside. Elastography-based ultrasound imaging techniques have received substantial attention in recent years due to their ability in detecting pathological tissue alterations non-invasively, which can substantially improve the capabilities of ultrasound imaging in both diagnosis and image-guided interventions.

Ultrasound Elastography (USE) has been explored for several clinical applications in recent years such as ablation guidance and monitoring [2] and breast lesion characterization [3]–[5]. USE is generally considered superior to ultrasound B-mode imaging and equal or superior to mammography in differentiating benign lesions from the malignant ones in the breast [6]–[9]. Surgical treatment of liver cancer [10]–[12], assessment of fibrosis in chronic liver diseases (CLD) [13], [14], differentiating benign thyroid nodules from malignant ones [15]–[18], detecting Prostate cancer [19], [20], differentiating abnormal lymph nodes in benign conditions [21] and brain tumor surgery [22], [23] are other clinical applications of USE.

The main idea behind USE techniques lies in monitoring tissue motion (induced by external stimuluses or internal forces often based on the pumping action of the heart), and inferring mechanical properties of the tissue from the motion. Estimation of tissue displacement is also referred to as time delay estimation (TDE), and is often performed using raw radio-frequency (RF) data. Different techniques of USE can be broadly grouped into dynamic and quasi-static elastography. Dynamic methods such as shear wave imaging (SWI) [24]–[26] and acoustic radiation force imaging (ARFI) [27] use Acoustic Radiation Force (ARF) to generate displacement in the tissue and can provide quantitative mechanical properties of tissue. However for quasi-static elastography, external excitation is performed by simply pressing ultrasound probe against tissue [28], [29] which can be done using a robotic arm [30], [31] or a hand-held probe (i.e. free-hand palpation) [32], [33]. In this paper, we focus on quasi-static free-hand palpation USE and compress the tissue in the axial direction, which inevitably creates deformation in both lateral and out of plane directions. While axial and lateral displacements can be calculated from 2D ultrasound images, estimation of out-of-plane movement requires 3D ultrasound images [34]–[36]. Displacement estimation is more accurate in the axial direction because of the high resolution of ultrasound images in this direction.

TDE methods can be broadly categorized into window-based and regularized optimization-based approaches. The problem of displacement estimation is ill-posed since the displacement of one sample by itself cannot be uniquely calculated [37]. In the window-based methods, a window is considered around the reference sample for which displacement is being estimated to change TDE to a well-posed problem. By assuming that all samples in the window have similar displacements, a corresponding window with similar sample values in the following image is located. Several similarity metrics are used to locate corresponding window such as maximization of the normalized cross correlation (NCC) of windows [38]–[40], phase-correlation wherein zero crossing

Morteza Mirzaei, Amir Asif and Hassan Rivaz are with the Department of Electrical and Computer Engineering, Concordia University, Montreal, QC, H3G 1M8, Canada. Email: m_irzae@encs.concordia.ca , amir.asif@concordia.ca and hrivaz@ece.concordia.ca

of phase determines displacement [41] and sum of absolute difference of windows [42]. Optimizing a regularized cost function is another approach for USE that impose smoothness regularization to make the problem well-posed [43]–[49]. These methods were computationally complex, but real-time USE based on regularized cost functions have recently been developed by exploiting Dynamic Programming and Analytic Minimization (DPAM) [50], [51] and GLobal Ultrasound Elastography (GLUE) [1]. These methods result in dense displacement and strain fields with the same size as the RF data. The main disadvantage of these methods is that utilizing quadratic regularization term leads to over-smoothed displacement fields.

Inspired by [37], we combine window-based and regularized optimization-based methods to increase robustness of the algorithm against noise which is abundant in free-hand USE due to out-of-plane movement, blood flow and other biological motions common in *in-vivo* data. The second major novelty of this paper is that we use total variation regularization (also known as the L1 norm regularization), which results in substantially sharper displacement maps. An iterative method is utilized for estimating the displacement, which further increases accuracy and robustness of the estimation against noise. We call our method tOtal Variation rEgulaRization and WINDow-based time-delay estimation (OVERWIND) and show that it outperforms both window-based and regularization-based approaches.

II. METHODS

Let I_1 and I_2 be the two frames of RF data collected as the tissue is undergoing some deformation. TDE entails estimating the displacement field between these two images. In this section, we first briefly describe the closely related previous work (GLUE) [1] and then present OVERWIND and derive equations to calculate TDE using this method.

A. GLUE: GLobal Ultrasound Elastography

In GLUE, the displacements are divided into integer and subsample displacement estimates. The initial integer displacement estimates come form Dynamic Programming (DP) [46]. The goal of GLUE is to calculate the subsample displacement component by minimizing the following cost function:

$$\begin{aligned} &C(\Delta a_{1,1}, \Delta l_{1,1}, , \ldots, \Delta a_{m,n}, \Delta l_{m,n}) = \\ &\Sigma_{j=1}^{n}\Sigma_{i=1}^{m}\{D(i, a_{i,j}, \Delta a_{i,j}, j, l_{i,j}, \Delta l_{i,j}) \\ &+R(i, a_{i,j}, \Delta a_{i,j}, j, l_{i,j}, \Delta l_{i,j})\} \end{aligned} \tag{1}$$

where the data term D is:

$$\begin{aligned} &D(i, a_{i,j}, \Delta a_{i,j}, j, l_{i,j}, \Delta l_{i,j}) = [I_1(i,j) \\ &-I_2(i + a_{i,j} + \Delta a_{i,j}, j + l_{i,j} + \Delta l_{i,j})]^2 \end{aligned}$$

and the regularization term R is:

$$\begin{aligned} &R(i, a_{i,j}, \Delta a_{i,j}, j, l_{i,j}, \Delta l_{i,j}) = \\ &\alpha_1(a_{i,j} + \Delta a_{i,j} - a_{i-1,j} - \Delta a_{i-1,j})^2 \\ &+\alpha_2(a_{i,j} + \Delta a_{i,j} - a_{i,j-1} - \Delta a_{i,j-1})^2 \\ &+\beta_1(l_{i,j} + \Delta l_{i,j} - l_{i-1,j} - \Delta l_{i-1,j})^2 \\ &+\beta_2(l_{i,j} + \Delta l_{i,j} - l_{i,j-1} - \Delta l_{i,j-1})^2. \end{aligned}$$

In these equations, I_1 and I_2 are pre- and post- compressed RF data of size $m \times n$. Notation $a_{i,j}$ and l_{ij} are axial and lateral integer displacements that are estimated by DP and $\Delta a_{i,j}$ and $\Delta l_{i,j}$ are axial and lateral subsample displacements that should be calculated. Finally, α_1, α_2, β_1 and β_2 are regularization parameters.

GLUE calculates the displacement estimates of all samples of the RF data simultaneously. As such, GLUE is relatively robust to local signal decorrelations since correlated areas guide the decorrelated regions. However, its displacement maps are very smooth, which leads to blurry strain images. In the next subsection, we increase robustness and also tackle problem of blurriness by introducing OVERWIND, which replaces the data term with a window-based term, and substitutes the regularization term with total variation regularization.

B. Utilizing Window-Based Data Terms

Inspired by [37], we combine window- and optimization-based methods to increase robustness of elastogram against noise by utilizing information available in the neighborhood of the reference sample. Therefore, for pixel (i, j), we consider a window of size $(2w_a+1)\times(2w_l+1)$ around sample (i, j) and assume that all samples in this neighborhood have the same displacement as sample (i, j), an assumption that is similar to the one used in the window-based methods. Therefore, the data term in Eq. (1) is replaced by

$$\begin{aligned} &D(i, a_{i,j}, \Delta a_{i,j}, j, l_{i,j}, \Delta l_{i,j}) = \\ &\tfrac{1}{(2w_a+1)(2w_l+1)}\Sigma_{k=-w_a}^{w_a}\Sigma_{r=-w_l}^{w_l}\big(I_1(i+k, j+r) \\ &-I_2(i+k+a_{i,j}+\Delta a_{i,j}, j+r+l_{i,j}+\Delta l_{i,j})\big)^2 \end{aligned}$$

The unknown variables Δa and Δl are now inside the "non-linear function"I_2, which means that the cost function cannot be optimized efficiently. To make the data term quadratic, we replace $I_2(i + k + a_{i,j} + \Delta a_{i,j}, j + r + l_{i,j} + \Delta l_{i,j})$ with its first order Taylor series expansion around $(i + k + a_{i,j}, j + r + l_{i,j})$. Furthermore, to simplify the notation, we denote $\frac{1}{(2w_a+1)(2w_l+1)}\Sigma_{k=-w_a}^{w_a}\Sigma_{r=-w_l}^{w_l}(.)$ as $\frac{1}{L}\Sigma_{k,r}(.)$ and $I_2(i + k + a_{i,j}, j + r + l_{i,j})$ as $I_2(.)$, so the data term can be rewritten as

$$\begin{aligned} D(i, a_{i,j}, \Delta a_{i,j}, j, l_{i,j}, \Delta l_{i,j}) = \frac{1}{L}\Sigma_{k,r}\Big(&I_1(i+k, j+r) \\ &-I_2(.) - \Delta a_{i,j}I'_{2a}(.) - \Delta l_{i,j}I'_{2l}(.)\Big)^2 \end{aligned} \tag{2}$$

where $I'_{2a}(.)$ and $I'_{2l}(.)$ are derivatives of I_2 in axial and lateral directions, respectively.

C. Using L1 Norm Regularization

The second issue of GLUE arises from the L2 norm regularization, which penalizes high gradients of displacement, and as such, prevents discontinuities in the displacement field. To cope with this problem, a non-quadratic regularization term should be utilized. The L1 norm regularization, which has a form of $\delta(s) = |s| = \sqrt{s^2}$ has optimal characteristic in terms of allowing sharp transitions. Although this regularization is convex, it is not differentiable at $s = 0$, which means that it cannot be efficiently optimized. A commonly used

technique to address this problem is to slightly perturb the regularization term around $s = 0$ [52]. In this paper, we use $\delta_x(s) = 2\lambda_x\sqrt{\lambda_x^2 + s^2}$ for regularization, where λ_x is a scaling parameter.

An inherent feature of regularization is that it reduces estimation variance at the cost of increased bias. In other words, we penalize the difference between $a_{i,j} + \Delta a_{i,j}$ and $a_{i-1,j} - \Delta a_{i-1,j}$, which leads to an underestimated displacement estimation. To prevent this kind of underestimation bias, ε_a and ε_l can be considered in the regularization term, where ε_a is the average of integer axial displacement difference between subsequent samples i and $i-1$ and ε_l is the average of integer lateral displacement difference between samples j and $j-1$ which are available from DP.

Inserting the proposed non-quadratic and unbiased regularization term, we have:

$$\begin{aligned} &R(i, a_{i,j}, \Delta a_{i,j}, j, l_{i,j}, \Delta l_{i,j}) = \\ &\alpha_1\delta_1(a_{i,j} + \Delta a_{i,j} - a_{i-1,j} - \Delta a_{i-1,j} - \varepsilon_a) \\ &+\alpha_2\delta_2(a_{i,j} + \Delta a_{i,j} - a_{i,j-1} - \Delta a_{i,j-1}) \\ &+\beta_1\delta_3(l_{i,j} + \Delta l_{i,j} - l_{i-1,j} - \Delta l_{i-1,j}) \\ &+\beta_2\delta_4(l_{i,j} + \Delta l_{i,j} - l_{i,j-1} - \Delta l_{i,j-1} - \varepsilon_l). \end{aligned} \tag{3}$$

Considering Eqs. (2) and (3), the final cost function can be presented as

$$\begin{aligned} &C(\Delta a_{1,1}, \dots, \Delta a_{m,n}) = \Sigma_{j=1}^{n}\Sigma_{i=1}^{m}\Bigg[\frac{1}{L}\Sigma_{k,r}\Big(I_1(i+k, j+r) \\ &-I_2(.) - \Delta a_{i,j}I'_{2a}(.) - \Delta l_{i,j}I'_{2l}(.)\Big)^2 \\ &+\alpha_1\delta_1(a_{i,j} + \Delta a_{i,j} - a_{i-1,j} - \Delta a_{i-1,j} - \varepsilon_a) \\ &+\alpha_2\delta_2(a_{i,j} + \Delta a_{i,j} - a_{i,j-1} - \Delta a_{i,j-1}) \\ &+\beta_1\delta_3(l_{i,j} + \Delta l_{i,j} - l_{i-1,j} - \Delta l_{i-1,j}) \\ &+\beta_2\delta_4(l_{i,j} + \Delta l_{i,j} - l_{i,j-1} - \Delta l_{i,j-1} - \varepsilon_l)\Bigg]. \end{aligned}$$

To find the optimal $\Delta a_{i,j}$ and $\Delta l_{i,j}$ values, one needs to differentiate C with respect to $\Delta a_{i,j}$ and $\Delta l_{i,j}$ and set the derivatives to zero, i.e. $\frac{\partial C}{\partial \Delta a_{i,j}} = 0$, and $\frac{\partial C}{\partial \Delta l_{i,j}} = 0$. To cope with the nonlinearity that $\delta'_x(s)$ will introduce to equations, we can use iterative methods wherein we assume $\vartheta = \dfrac{1}{\sqrt{\lambda_x^2 + s^2}}$ is fixed and equations are linear in each iteration. After every iteration, ϑ will use the updated value in the previous iteration. In this case by stacking all $2mn$ unknown parameters in a vector as $\Delta d_{2m\times n} = [\Delta a_{1,1}, \Delta l_{1,1}\Delta a_{1,2}, \Delta l_{1,2}, \cdots, \Delta a_{m,n}, \Delta l_{m,n}]^{\mathrm{T}}$, the following linear equation should be solved to obtain the optimal subsample displacements

$$(H + D)\Delta d = \frac{1}{L}\Sigma_{k,r}(P\mu) - Dd - b_1\varepsilon_a - b_2\varepsilon_l \tag{4}$$

where

$$H = \mathrm{diag}\{h(1,1), \cdots, h(1,n), \cdots, h(m,1), \cdots, h(m,n)\}$$

and $h(i,j)$ is a 2×2 matrix as

$$h(i,j) = \begin{bmatrix} \frac{1}{L}\Sigma_{k,r}(I'_{2a}(.))^2 & \frac{1}{L}\Sigma_{k,r}(I'_{2a}(.)I'_{2l}(.)) \\ \frac{1}{L}\Sigma_{k,r}(I'_{2a}(.)I'_{2l}(.)) & \frac{1}{L}\Sigma_{k,r}(I'_{2l}(.))^2 \end{bmatrix}.$$

P is a diagonal matrix as

$$P = \mathrm{diag}\{e(1,1), \cdots, e(1,n), \cdots, e(m,1), \cdots, e(m,n)\}$$

where $e(i,j)$ is a 2×2 matrix as

$$e(i,j) = \begin{bmatrix} I'_{2a}(.) & 0 \\ 0 & I'_{2l}(.) \end{bmatrix}.$$

μ is a vector as

$$\mu = [g_{1,1}, g_{1,2}, \cdots, g_{m,n}]^{\mathrm{T}} \otimes [1,1]^{\mathrm{T}}$$

where $g_{i,j}$ is subtraction of two images as

$$g_{i,j} = I_1(i+k, j+r) - I_2(.)$$

and $\otimes$ is Kronecker tensor product. The matrix D can be organized as

$$D = \begin{bmatrix} Q_1 & R_1 & 0 & 0 & \dots & \dots & 0 \\ R_1 & S_1 & R_2 & 0 & 0 & \dots & 0 \\ 0 & R_2 & S_2 & R_3 & 0 & \ddots & \vdots \\ \vdots & \ddots & \ddots & \ddots & \ddots & \ddots & \vdots \\ 0 & 0 & 0 & R_{m-3} & S_{m-3} & R_{m-2} & 0 \\ 0 & 0 & 0 & \ddots & R_{m-2} & S_{m-2} & R_{m-1} \\ 0 & \dots & \dots & 0 & 0 & R_{m-1} & Q_2 \end{bmatrix}$$

where Q_1, Q_2 and $S_z,\ z \in \{1, \cdots, m-2\}$ are pentadiagonal matrices with the following structure

$$\begin{bmatrix} * & 0 & * & & & & \\ 0 & * & 0 & * & & 0 & \\ * & 0 & * & 0 & * & & \\ & \ddots & \ddots & \ddots & \ddots & \ddots & \\ & & * & 0 & * & 0 & * \\ & 0 & & * & 0 & * & 0 \\ & & & & * & 0 & * \end{bmatrix}$$

with the main diagonals (md) given in Eqs. (8) and (9). The first upper/lower diagonals are zero, while the second upper/lower diagonals (sd) are

$$\begin{aligned} Q_{1\mathrm{sd}} = &\ -\big[\Theta_2(1,2), \Gamma_2(1,2), \cdots, \Theta_2(1,n), \Gamma_2(1,n)\big]^{\mathrm{T}}, \\ Q_{2\mathrm{sd}} = &\ -\big[\Theta_2(m,2), \Gamma_2(m,2), \cdots, \Theta_2(m,n), \Gamma_2(m,n)\big]^{\mathrm{T}}, \\ S_{z\mathrm{sd}} = &\ -\big[\Theta_2(z+1,2), \Gamma_2(z+1,2), \\ &\cdots, \Theta_2(z+1,n), \Gamma_2(z+1,n)\big]^{\mathrm{T}} \end{aligned}$$

where

$$\begin{aligned} \Theta_1(i,j) &= \frac{\alpha_1\lambda_1}{\sqrt{\lambda_1^2 + (a_{i,j} + \Delta a_{i,j} - a_{i-1,j} - \Delta a_{i-1,j} - \varepsilon)^2}}, \\ \Theta_2(i,j) &= \frac{\alpha_2\lambda_2}{\sqrt{\lambda_2^2 + (a_{i,j} + \Delta a_{i,j} - a_{i,j-1} - \Delta a_{i,j-1})^2}}, \\ \Gamma_1(i,j) &= \frac{\beta_1\lambda_3}{\sqrt{\lambda_3^2 + (l_{i,j} + \Delta l_{i,j} - l_{i-1,j} - \Delta l_{i-1,j})^2}}, \\ \Gamma_2(i,j) &= \frac{\beta_2\lambda_4}{\sqrt{\lambda_4^2 + (l_{i,j} + \Delta l_{i,j} - l_{i,j-1} - \Delta l_{i,j-1})^2}}. \end{aligned}$$

$R_\kappa,\ \kappa \in \{1, \cdots, m-1\}$, are diagonal matrices with the main diagonal given by

$$-\big[\Theta_1(\kappa+1,1), \Gamma_1(\kappa+1,1), \cdots, \Theta_1(\kappa+1,n), \Gamma_1(\kappa+1,n)\big]^{\mathrm{T}}.$$

Finally vectors b_1 and b_2 are defined in Eq. (10).

The OVERWIND code is currently implemented in Matlab and takes 2.9 seconds on a 3.20 GHz i7 Intel CPU for an image of size 1000×100. By implementing OVERWIND in C and using graphics cards, it can achieve real-time performance.

In the final step, the estimated displacement field is spatially differentiated to calculate strain. In particular, a least squares regression technique is used to limit the effect of noise on the gradient operator.

III. Results

OVERWIND combines window-based methods with regularized optimization-based techniques. To illustrate its performance, we compare it to NCC (a pure window-based method) and GLUE (a pure regularized optimization-based method) on data collected from simulations, phantom and *in-vivo* experiments. For comparison to GLUE, the publicly available GLUE code is used. NCC is straightforward to implement, but suffers from sensitivity to signal de-correlation and false peaks which occur when a secondary NCC peak or zero crossing of phase or sum of absolute difference exceeds the true ones. To reduce the chance of false peaks, time-domain cross correlation with prior estimates (TDPE) is introduced in [40] which is also utilized in this paper to complement NCC with windows of size (10×4) λ and 86% overlap of windows. In addition, 3-point parabolic interpolation is used to find the 2D sub-sample location of the correlation peak. The results of NCC with a spline-based interpolation method to find the subsample displacement estimates are shown in the Supplementary Material, available in the supplementary files/multimedia tab. In TPDE, only a small part of post compressed RF data should be searched for correlated window and the searching area is limited to a neighborhood around the previous time-delay estimate. To improve the results of NCC, we up-sample the RF data using 2D splines by a factor of 10 in both dimensions and down-sample estimated displacement from NCC using 2D splines by a factor of $1/10$. This significantly improves the results at a cost of increased computational complexity by a factor of more than 100. The Signal to Noise Ratio (SNR) and Contrast to Noise Ratio (CNR) are also considered to highlight differences in the outputs of the two approaches quantitatively. The SNR and CNR are computed according to [53]:

$$SNR = \frac{\bar{s}}{\sigma}, \qquad \text{CNR} = \sqrt{\frac{2(\bar{s}_b - \bar{s}_t)^2}{\sigma_b^2 + \sigma_t^2}}, \tag{5}$$

where $\bar{s}_t$ and $\bar{s}_b$ are averages of strain in the target and background windows, σ_b^2 and σ_t^2 are variances of the strain in the target and background windows, and $\bar{s}$ and σ are the average and standard deviation of strain over small windows, respectively. It is important to note that each window should be large enough to ensure statistically meaningful values of mean and variance, and should be located in a region where the ground truth strain is uniform within the window.

A. Simulation Data

The first simulation experiment has a sharp change in the displacement field to highlight the differences between GLUE and OVERWIND. All samples of the image have a displacement of zero, except for a rectangle in the middle which is moved by two pixels as shown in Fig. 1(a).

In the next step, a homogeneous phantom with a cylindrical inclusion with zero stiffness as shown in Fig. 2 is considered. The inclusion simulates a vein which has little resistance to compression. Ultrasound images are generated using the Field II ultrasound simulation software [54] by considering slightly more than 10 scatterers per mm^3 to satisfy Rayleigh scattering regime [55]. Deformations are computed using the ABAQUS FEM software package (Providence, RI, USA). For computing displacement of scatterers, the phantom is meshed and compressed using finite element simulation to get the 3D displacement of each node of the mesh. The displacement of each scatterer is then calculated by interpolating the displacement of its neighboring nodes.

Two additional phantoms are simulated for a more thorough comparison between the proposed method and GLUE, and the results are provided in the Supplementary Material, available in the supplementary files/multimedia tab.

B. Simulation Results

For the first simple simulation experiment, the estimated displacement fields obtained from GLUE and OVERWIND are shown in Fig. 1(b) and (c), respectively. This example clearly illustrate the limitation of the L2 norm in GLUE, which puts very heavy penalty in sharp changes in the displacement field because of the power 2. Whereas the L1 norm in OVERWIND tolerates sharp changes in displacement, and as such, creates a displacement field that is very sharp.

In the second simulation study, the simulated phantom is compressed by 1% and the resulting strain images estimated by NCC, GLUE and OVERWIND are shown in Fig. 3. The OVERWIND strain image is the closest one to the ground-truth strain, especially around the inclusion where its edges are substantially sharper. To better compare the results, the Edge Spread Functions (ESF) of the estimated strain fields across two vertical and horizontal lines of Fig. 3 (a) are depicted in Fig. 4. It is further clarified from these plots that the ESF of OVERWIND is substantially closer to the ground truth as compared to both NCC and GLUE. The ESF of all horizontal and vertical lines which pass through the target window are shown in the Supplementary Material, available in the supplementary files/multimedia tab.

To compare the sensitivity of different methods against noise, we add two levels of Gaussian noise with peak signal-to-noise ratio (PSNR) values of 20 and 16.4 to the simulated RF data. NCC fails to estimate strain given the large energy of noise, and therefore, only the results of GLUE and OVERWIND are shown in Fig. 5. It is clear that the strain image of OVERWIND substantially outperforms that of GLUE.

To quantitatively compare the results, the SNR and CNR of strain images are shown in Table I. For calculating these values, we ran a Monte Carlo simulation by estimating strains 1000 times with different random noise realizations. The mean and standard deviation (std) of SNR and CNR for these 1000 experiments are reported for different levels of noise. As seen from Figs. 3 and 5, and Table I not only OVERWIND

$$Q_{1\text{md}} = \begin{bmatrix} \Theta_1(2,1)+\Theta_2(1,2) \\ \Gamma_1(2,1)+\Gamma_2(1,2) \\ \Theta_1(2,2)+\Theta_2(1,2)+\Theta_2(1,3) \\ \Gamma_1(2,2)+\Gamma_2(1,2)+\Gamma_2(1,3) \\ \vdots \\ \Theta_1(2,n-1)+\Theta_2(1,n-1)+\Theta_2(1,n) \\ \Gamma_1(2,n-1)+\Gamma_2(1,n-1)+\Gamma_2(1,n) \\ \Theta_1(2,n)+\Theta_2(1,n) \\ \Gamma_1(2,n)+\Gamma_2(1,n) \end{bmatrix}, Q_{2\text{md}} = \begin{bmatrix} \Theta_1(m,1)+\Theta_2(m,2) \\ \Gamma_1(m,1)+\Gamma_2(m,2) \\ \Theta_1(m,2)+\Theta_2(m,2)+\Theta_2(m,3) \\ \Gamma_1(m,2)+\Gamma_2(m,2)+\Gamma_2(m,3) \\ \vdots \\ \Theta_1(m,n-1)+\Theta_2(m,n-1)+\Theta_2(m,n) \\ \Gamma_1(m,n-1)+\Gamma_2(m,n-1)+\Gamma_2(m,n) \\ \Theta_1(m,n)+\Theta_2(m,n) \\ \Gamma_1(m,n)+\Gamma_2(m,n) \end{bmatrix}, \tag{8}$$

$$S_{z\text{md}} = \begin{bmatrix} \Theta_1(z+1,1)+\Theta_1(z+2,1)+\Theta_2(z+1,2) \\ \Gamma_1(z+1,1)+\Gamma_1(z+2,1)+\Gamma_2(z+1,2) \\ \Theta_1(z+1,2)+\Theta_1(z+2,2)+\Theta_2(z+1,2)+\Theta_2(z+1,3) \\ \Gamma_1(z+1,2)+\Gamma_1(z+2,2)+\Gamma_2(z+1,2)+\Gamma_2(z+1,3) \\ \vdots \\ \Theta_1(z+1,n-1)+\Theta_1(z+2,n-1)+\Theta_2(z+1,n-1)+\Theta_2(z+1,n) \\ \Gamma_1(z+1,n-1)+\Gamma_1(z+2,n-1)+\Gamma_2(z+1,n-1)+\Gamma_2(z+1,n) \\ \Theta_1(z+1,n)+\Theta_1(z+2,n)+\Theta_2(z+1,n) \\ \Gamma_1(z+1,n)+\Gamma_2(z+2,n)+\Gamma_2(z+1,n) \end{bmatrix}, \tag{9}$$

$$\begin{gathered} b_1 = [\Theta_1(2,1), 0, \cdots, \Theta_1(2,n), 0, \Theta_1(3,1)-\Theta_1(2,1), 0, \cdots, \Theta_1(3,n)-\Theta_1(2,n), 0, \cdots, \Theta_1(m,1)-\Theta_1(m-1,1), 0, \cdots, \\ \Theta_1(m,n)-\Theta_1(m-1,n), 0, -\Theta_1(m,1), 0, \cdots, -\Theta_1(m,n), 0] \\ b_2 = [0, \Gamma_2(2,1), \cdots, 0, \Gamma_2(2,n), 0, \Gamma_2(3,1)-\Gamma_2(2,1), \cdots, 0, \Gamma_2(3,n)-\Gamma_2(2,n), \cdots, 0, \Gamma_2(m,1)-\Gamma_2(m-1,1), \cdots \\ , 0, \Gamma_2(m,n)-\Gamma_2(m-1,n), 0, -\Gamma_2(m,1), \cdots, 0, -\Gamma_2(m,n)] \end{gathered} \tag{10}$$

TABLE I: Mean and standard deviation of SNR and CNR for 1000 strain images of the simulated phantom for different methods and noise levels. Windows that are considered for calculating CNR are shown in white and black lines in Fig. 3. The white window is considered for calculation of SNR. The mean improvement of OVERWIND compared to GLUE is also reported for each level of noise.

PSNR		SNR mean (std)	CNR mean (std)
∞ (No noise)	NCC	2.05 (-)	17.07 (-)
	GLUE	2.61 (-)	23.51 (-)
	OVERWIND	3.09 (-)	28.51 (-)
	Improvement	**18.39**%	**21.26**%
20	NCC	fails	fails
	GLUE	2.14 (0.72)	18.79 (2.89)
	OVERWIND	2.92 (0.52)	25.51 (3.30)
	Improvement	**31.77**%	**33.26**%
16.4	NCC	fails	fails
	GLUE	fails	fails
	OVERWIND	1.59 (0.97)	18.37 (5.06)
	Improvement	-	-

outperforms GLUE for each level of noise, but also has more robust performance against increasing the amplitude of noise.

C. Experimental Data

The phantom experiment is carried out at PERFORM centre, Concordia University. RF data is acquired from a model 059 tissue mimicking breast phantom (CIRS, Norfolk, VA, USA) using an E-Cube R12 ultrasound machine (Alpinion, Bothell, WA, USA) with a L3-12H probe operating at the center frequency of 7.27 MHz and sampling frequency of 40 MHz.

For the clinical study, we analyze data from three patients with liver cancer. The data was collected at the Johns Hopkins hospital with an Antares ultrasound machine (Siemens, Issaquah, WA, USA) using a VF10-5 linear probe with a center frequency of 6.6 MHz and sampling frequency of 40 MHz. The study was approved by the ethics institutional review board at Johns Hopkins University.

D. Phantom Results

For the phantom data, strain images estimated by NCC, GLUE and OVERWIND are shown in Fig. 6. The estimated strain by GLUE suffers from artifacts and regularization weights should be increased to remove these artifacts. However, by increasing the regularization weights, more blurriness especially on the edges of the inclusion is generated. OVERWIND produces a much smoother image than other methods

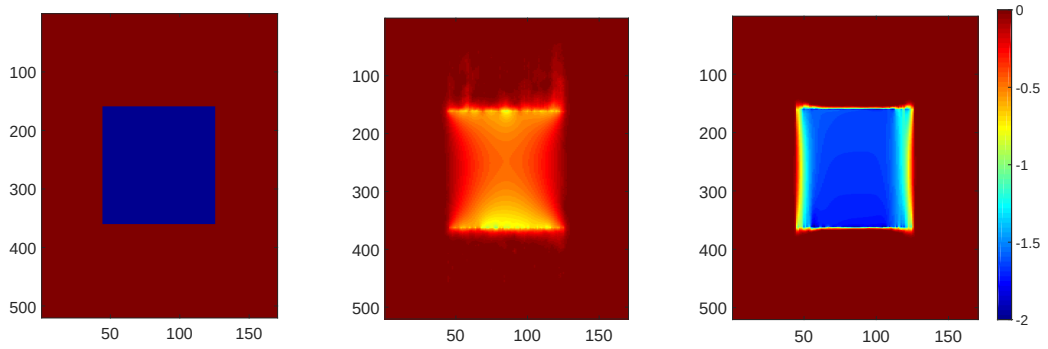

(a) Ground truth (b) GLUE (c) OVERWIND

Fig. 1: Comparison of GLUE and OVERWIND in a simulation experiment. In comparison to the ground-truth displacement in (a), the displacement field estimated by GLUE in (b) is not sharp and also underestimates the magnitude of displacement. In contrast, the result of OVERWIND is sharp and also more similar to the ground truth.

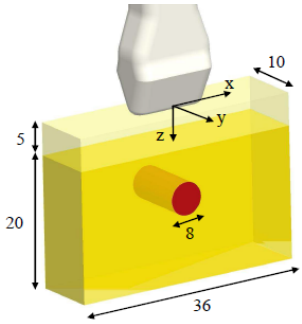

Fig. 2: Schematic of the simulated phantom by Field II with the simulated vein in the middle with zero stiffness (reproduced from [51]).

while preserving the sharpness of edges. For comparing the ESF plots, we consider two perpendicular lines in the strain profile of NCC, GLUE and OVERWIND shown as black lines in Fig. 6 (c) and illustrate the calculated strain profiles across these lines. The results presented in Fig. 7, demonstrate that OVERWIND is less noisy and sharper around the edges. The ESF of all horizontal and vertical lines that pass through the target window are shown in the Supplementary Material, available in the supplementary files/multimedia tab. It can be seen from Fig. 6 that the strain values at the right and left side of the phantom are not equal. This is caused by applying a compression that is not purely axial and likely contains some in-plane rotation, which is possible in hand-held compressions.

For a comprehensive CNR and SNR comparison, the results of histogram analysis are shown in Fig. 7. The target and background windows considered for CNR and SNR calculation are shown in Fig. 6 (a). We have moved the small red window within the large red window to take 9 target windows. At the same time, the small blue window is swiped within the large blue window to consider 24 background windows. CNR is calculated for every combination of target and background windows, resulting in 216 values. SNR is calculated for all 24 background windows. Fig. 7 shows the distribution of the aforementioned CNR and SNR values. It is clear from these histograms that OVERWIND produces strain images with higher SNR and CNR. The mean of 216 CNR values are 15.40, 6.31 and 6.28 for OVERWIND, GLUE and NCC, respectively. Moreover, the mean of 24 SNRs are 42.7, 12.77 and 16.72 for OVERWIND, GLUE and NCC, respectively.

E. In-vivo Results

NCC fails in estimating strains for this *in-vivo* data and therefore only the results of GLUE and OVERWIND are presented in Figs. 8, 9 and 10. While the strain images clearly show the tumor in these three patients, the B-mode image hardly shows the tumor especially in patients 1 and 3.

The OVERWIND strain images are much smoother than GLUE while preserving the sharp edges of the tumors and the veins. For quantitative comparison of two methods, the CNR and SNR of the strains are calculated and the results are presented in Table II, which also corroborate better performance of OVERWIND.

In the last experiment, data collected from patient 3 shows the left anterior branch of portal vein. This vein is marked by the symbol 'A' in Fig. 10-(a) and has low pressure. Therefore, it compresses easily during free-hand palpation, which results in high strain values. The boundaries of the veins are substantially sharper in the OVERWIND strain image.

In the Supplementary Material (available in the supplementary files/multimedia tab), we compare the results of GLUE and OVERWIND for different regularization weights. These results show that both methods generate smoother strain images with higher regularization weights as expected. However, OVERWIND generates substantially sharper strain estimates at the boundaries of different types of tissue, and smoother strain estimates in homogenous regions.

IV. Discussion

In this paper, a method named OVERWIND is proposed for ultrasound elastography. OVERWIND generates displacement estimation fields that are smooth in uniform regions and sharp at boundaries of two mediums, which was not possible with previous techniques such as GLUE or NCC.

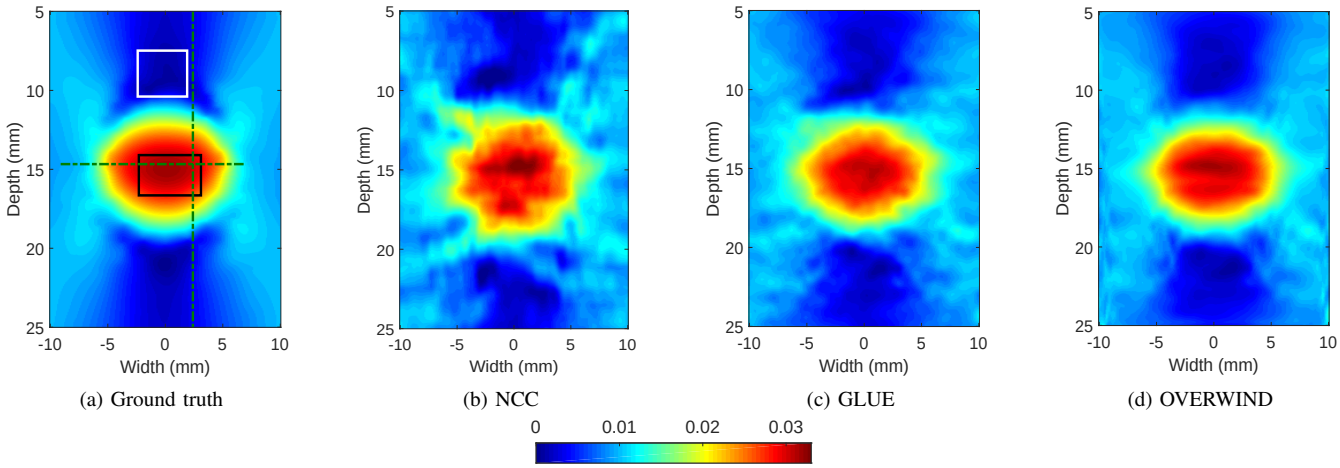

(a) Ground truth (b) NCC (c) GLUE (d) OVERWIND

Fig. 3: Strain estimated by three methods in the FEM simulated phantom. The black and white boxes in (a) are used as the foreground and background windows respectively for calculating CNR. The dashed-dotted horizontal and vertical lines in (a) are used for plotting the edge spread function of Fig. 4.

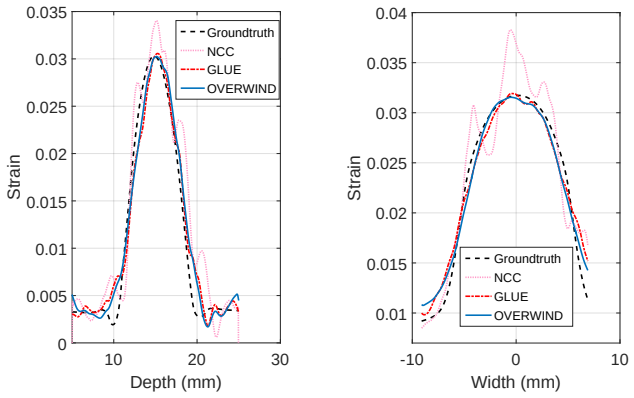

(a) Vertical (b) Horizontal

Fig. 4: Edge spread function of NCC, GLUE and OVERWIND for the FEM simulated phantom across two perpendicular lines shown in Fig. 3 (c).

TABLE II: SNR and CNR values in calculated strain fields of two patients. Windows that are considered for calculating CNR are shown in Figs. 8, 9 and 10 and only black windows are considered for SNR.

	SNR		CNR	
	OVERWIND	GLUE	OVERWIND	GLUE
P1	11.54	10.31	8.97	7.67
P2	13.90	7.69	10.48	5.92
P3	8.37	4.46	4.81	2.59
Average	11.27	7.48	8.08	5.39
Improvement	**50.66%**		**49.90%**	

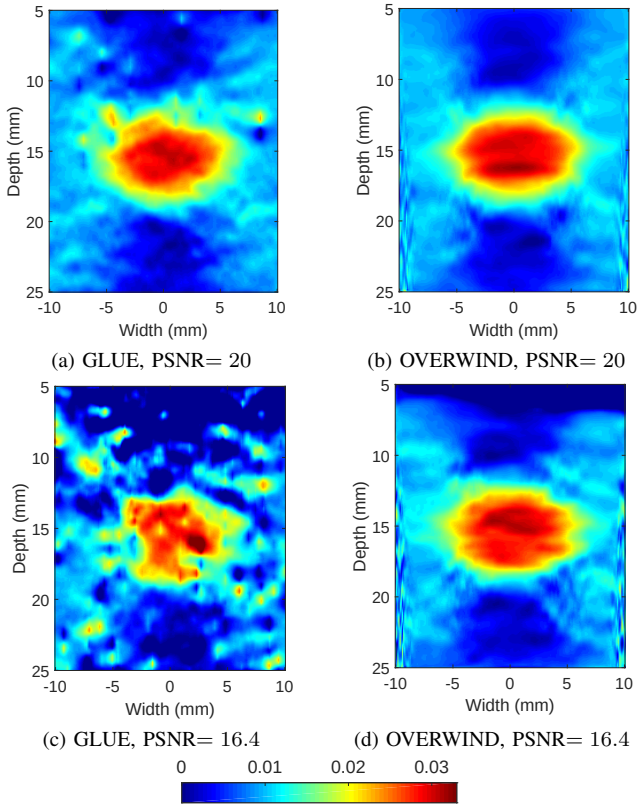

(a) GLUE, PSNR= 20 (b) OVERWIND, PSNR= 20

(c) GLUE, PSNR= 16.4 (d) OVERWIND, PSNR= 16.4

Fig. 5: Estimated strain images in the FEM simulation experiment by adding Gaussian noise to pre- and post-compressed RF data.

In OVERWIND, a cost function containing two parts is introduced for optimal displacement estimation. In the first part of the proposed cost function, the difference of two images as pre- and post- compressed RF data are penalized. By assuming that neighboring samples have the same displacement, small windows are considered around each sample and all samples in these windows are forced to have the same displacement in

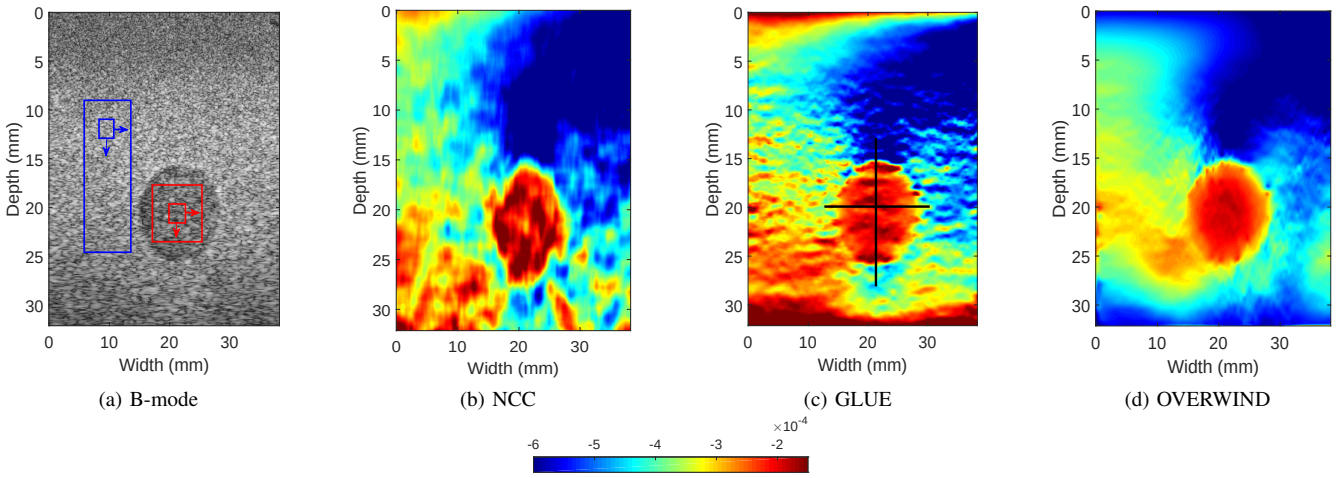

(a) B-mode (b) NCC (c) GLUE (d) OVERWIND

Fig. 6: B-mode and strain images of the CIRS phantom.

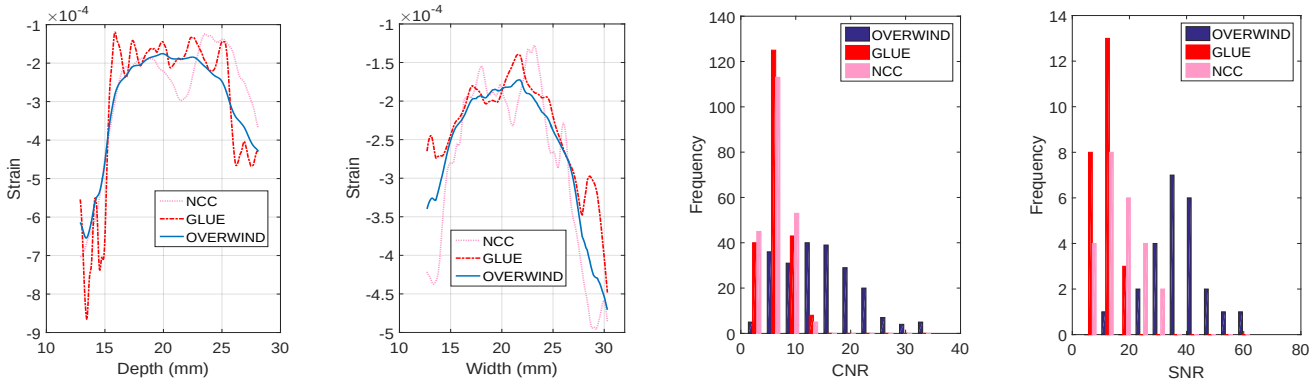

(a) Vertical ESF (b) Horizontal ESF (c) CNR Histogram (d) SNR Histogram

Fig. 7: Edge spread function of estimated strains by NCC, GLUE and OVERWIND in the CIRS phantom experiment across two perpendicular lines specified in Fig. 6 (c) are shown in (a) and (b). Histograms of CNR (c) and SNR (d) for estimated strains by NCC, GLUE and OVERWIND for all 216 combination of target and background windows that are shown in Fig. 6 (a).

the pre- and post-compression RF data. Therefore, this method increases robustness against noise by utilizing information from neighboring samples. Noise is a significant detrimental factor in free-hand palpation elastography. An example that increases noise is the out-of-plane motion in the images especially when the probe has to be held at difficult angles in the *in-vivo* experiments. Other sources of noise are blood flow and biological motions and heat generated in the ablation procedures. Therefore, robust methods play an important role in wider adoption of ultrasound elastography. The proposed OVERWIND method successfully estimated strains for simulation data with added noise and phantom data as well as *in-vivo* data that are intrinsically noisy.

The background in the phantom experiment does not show uniform strain for three main reasons. First, there is an important distinction between strain and elasticity modulus. Even in a simulation experiment with perfectly uniform background and uniform axial compression, the strain values vary significantly. Second, the compression is applied by hand and therefore the right and left hand side of the image may experience different compression levels. And third, the breast phantom is not cubic and due to its curved surface, different compression levels are applied at different locations.

The second term of cost function deals with regularization which penalizes displacement of neighbor samples. In the previous methods like GLUE, a quadratic term of displacement differences is utilized which causes over-smoothing. An intuitive reason for over-smoothing is that a change in displacement, for example, of 3 samples will result in a large penalty of $3^2 = 9$. Therefore, the L2 norm regularization tries to break down this large transition to 3 changes, each at 1 sample to incur a smaller penalty of $1+1+1 = 3$, which leads to blurry edges. Herein, we changed the regularization term to the L1 norm which assigns a smaller penalty to discontinuities. This modification added nonlinear terms to the cost function, and therefore, we used iterative methods to optimize the cost function. Results that are presented in this paper are obtained in 5 iterations. Utilizing the L1 norm also introduces a scaling parameter that strikes a balance between sharpness and robustness to noise. As is shown in the Results Section, GLUE suffers from artifacts that can be reduced by increasing regularization weights, which has a negative impact of losing information especially in edges. However, in OVERWIND, there is a tradeoff between regularization weights and scaling

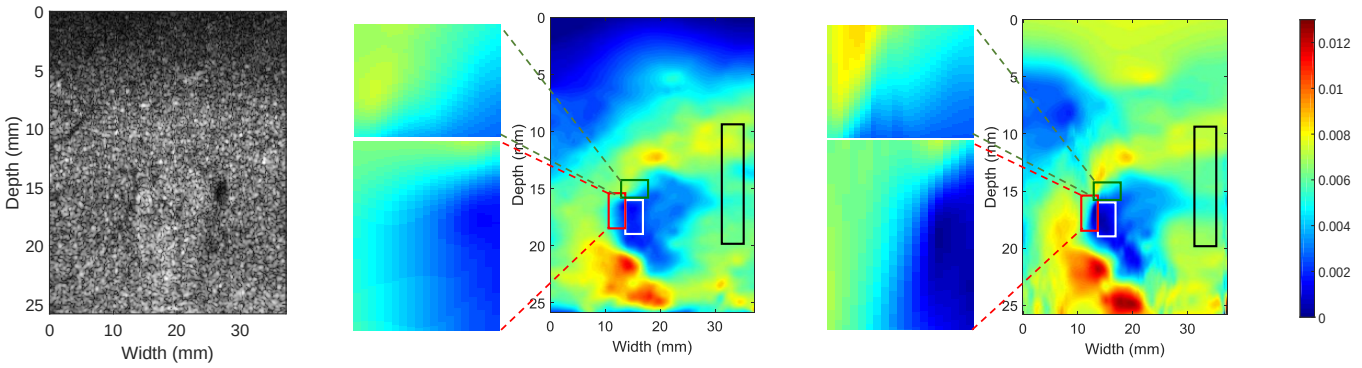

(a) B-mode (b) GLUE (c) OVERWIND

Fig. 8: B-mode and strain images of patient 1 (P1).

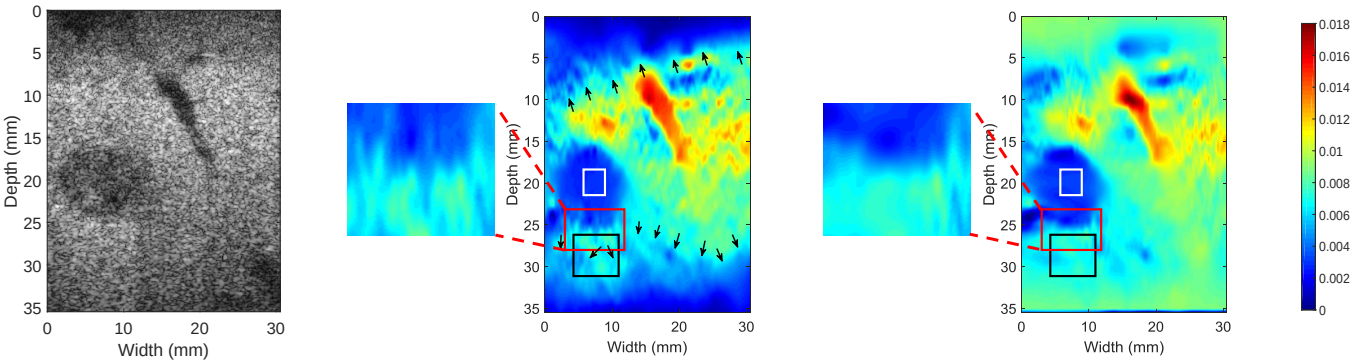

(a) B-mode (b) GLUE (c) OVERWIND

Fig. 9: B-mode and strain images of patient 2 (P2).

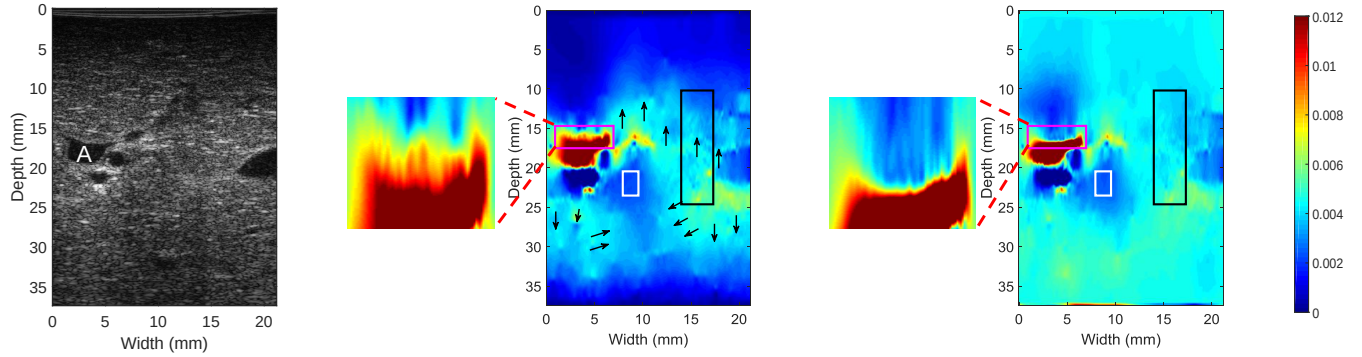

(a) B-mode (b) GLUE (c) OVERWIND

Fig. 10: B-mode and strain images of patient 3 (P3).

parameters which can remove artifacts much more than GLUE by increasing regularization weights while preserving useful information in edges by properly tuning the scaling parameter.

OVERWIND provides denser estimation for all samples of RF data, in contrast to window-based methods that provide displacement estimates for larger windows. Therefore, it is more suitable for imaging small targets. In addition, OVERWIND does not blur the boundaries, which reduces the detectability of small targets.

A concern regarding OVERWIND is the size of equations and memory amount that is required to store parameters because it deals with large matrices of size $2mn \times 2mn$. For a typical RF frame of size 1000×100, this matrix will be of size 200000×200000 needing 298 GB of memory for storage in double precision floating point format. Fortunately, most elements of these matrices are zero, and as such, they can be stored as sparse matrices to reduce memory load. As an example, left hand side of Eq. (4) for a typical RF frame of size 1000×100 needs only 19.73 MB and the right hand side uses 1.52 MB of memory, if they are stored as sparse matrices.

For differentiation of each sample, a window of size $(2\rho+1) \times 1$ has been considered around the reference sample. Utilizing the least square method, a line is fitted to these samples and its slope is regarded as the strain value of that sample. Moving the center of the window one step forward,

strain of the next sample will be calculated. It is clear that a large value for ρ makes the image smoother at the cost losing information, while a small ρ may increase noise in strain estimation. We used windows of length 53, 63 and 83 (i.e. $\rho = 26$, $\rho = 31$ and $\rho = 41$) for simulation, phantom and *in-vivo* results, respectively. In our previous method DPAM [51], we proposed a Kalman filter for estimating a strain image that is sharp at boundaries of different tissues and smooth in homogenous regions. OVERWIND also has the same final goal, but it achieves this goal by estimating a high-quality displacement image. In other words, Kalman filter is a post-processing technique applied on noisy displacement estimates to estimate sharp strain estimates. To show that OVERWIND is superior to DPAM and Kalman filtering, we show the results of simulation, phantom and *in-vivo* experiments in the Supplementary Material, available in the supplementary files/multimedia tab.

V. Conclusion

In this paper we proposed a novel method for real time ultrasound elastography. We coupled the two well-known window-based and regularized optimization-based methods to increase robustness against noise. Another advantage of the proposed method was utilizing the total variation L1 norm regularization instead of the L2 norm regularization, which results in sharper strain images. We compared the performance of our approach with GLUE and NCC on data collected from simulations, phantom set-ups, and *in-vivo* experiments.

Acknowledgment

This work was supported by Natural Science and Engineering Research Council of Canada (NSERC) Discovery Grants RGPIN-2015-04136 and RGPIN-2017-06629. The *in-vivo* data of liver patient was collected at Johns Hopkins Hospital. Authors would like to thank the principal investigators Drs. E. Boctor, M. Choti and G. Hager for sharing the data with us. The RF data of mimicking phantom was collected at Concordia University's PERFORM Centre with an Alpinion ultrasound machine. The authors would like to thank Julian Lee from Alpinion USA for his technical help.

References

[1] H. S. Hashemi and H. Rivaz, "Global time-delay estimation in ultrasound elastography," *IEEE Transactions on Ultrasonics, Ferroelectrics, and Frequency Control*, vol. 64, no. 10, pp. 1625–1636, 2017.

[2] R. M. Sigrist, J. Liau, A. El Kaffas, M. C. Chammas, and J. K. Willmann, "Ultrasound elastography: review of techniques and clinical applications," *Theranostics*, vol. 7, no. 5, p. 1303, 2017.

[3] T. Hall, Y. Zhu, C. S. Spalding, and L. T. Cook, "In vivo results of real-time freehand elasticity imaging," in *2001 IEEE Ultrasonics Symposium. Proceedings. An International Symposium (Cat. No.01CH37263)*, vol. 2, 2001, pp. 1653–1657.

[4] M. Doyley, J. Bamber, F. Fuechsel, and N. Bush, "A freehand elastographic imaging approach for clinical breast imaging: system development and performance evaluation," *Ultrasound in Medicine and Biology.*, vol. 27, no. 10, pp. 1347–1357, 2001.

[5] N. Uniyal, H. Eskandari, P. Abolmaesumi, S. Sojoudi, P. Gordon, L. Warren, R. N. Rohling, S. E. Salcudean, and M. Moradi, "Ultrasound rf time series for classification of breast lesions," *IEEE Transactions on Medical Imaging*, vol. 34, no. 2, pp. 652–661, 2015.

[6] H. Zhi, B. Ou, B.-M. Luo, X. Feng, Y.-L. Wen, and H.-Y. Yang, "Comparison of ultrasound elastography, mammography, and sonography in the diagnosis of solid breast lesions," *Journal of ultrasound in medicine*, vol. 26, no. 6, pp. 807–815, 2007.

[7] L. Leong, L. Sim, Y. Lee, F. Ng, C. Wan, S. Fook-Chong, A. Jara-Lazaro, and P. Tan, "A prospective study to compare the diagnostic performance of breast elastography versus conventional breast ultrasound," *Clinical radiology*, vol. 65, no. 11, pp. 887–894, 2010.

[8] K. M. Hiltawsky, M. Krüger, C. Starke, L. Heuser, H. Ermert, and A. Jensen, "Freehand ultrasound elastography of breast lesions: clinical results," *Ultrasound in medicine & biology*, vol. 27, no. 11, pp. 1461–1469, 2001.

[9] A. Thomas, T. Fischer, H. Frey, R. Ohlinger, S. Grunwald, J.-U. Blohmer, K.-J. Winzer, S. Weber, G. Kristiansen, B. Ebert *et al.*, "Real-time elastographyan advanced method of ultrasound: first results in 108 patients with breast lesions," *Ultrasound in Obstetrics and Gynecology*, vol. 28, no. 3, pp. 335–340, 2006.

[10] H. Rivaz, E. M. Boctor, M. A. Choti, and G. D. Hager, "Ultrasound elastography using multiple images," *Medical Image Analysis*, vol. 18, no. 2, pp. 314 – 329, 2014.

[11] W. Yang, M. Alexander, N. Rubert, A. Ingle, M. Lubner, T. Ziemlewicz, J. L. Hinshaw, F. T. Lee, J. A. Zagzebski, and T. Varghese, "Monitoring microwave ablation for liver tumors with electrode displacement strain imaging," in *2014 IEEE International Ultrasonics Symposium*, 2014, pp. 1128–1131.

[12] N. Frulio and H. Trillaud, "Ultrasound elastography in liver," *Diagnostic and Interventional Imaging*, vol. 94, no. 5, pp. 515 – 534, 2013.

[13] M. Friedrich-Rust, M.-F. Ong, S. Martens, C. Sarrazin, J. Bojunga, S. Zeuzem, and E. Herrmann, "Performance of transient elastography for the staging of liver fibrosis: a meta-analysis," *Gastroenterology*, vol. 134, no. 4, pp. 960–974, 2008.

[14] E. Tsochatzis, K. Gurusamy, S. Ntaoula, E. Cholongitas, B. Davidson, and A. Burroughs, "Elastography for the diagnosis of severity of fibrosis in chronic liver disease: a meta-analysis of diagnostic accuracy," *Journal of hepatology*, vol. 54, no. 4, pp. 650–659, 2011.

[15] Y. Hong, X. Liu, Z. Li, X. Zhang, M. Chen, and Z. Luo, "Real-time ultrasound elastography in the differential diagnosis of benign and malignant thyroid nodules," *Journal of Ultrasound in Medicine*, vol. 28, no. 7, pp. 861–867, 2009.

[16] P. Trimboli, R. Guglielmi, S. Monti, I. Misischi, F. Graziano, N. Nasrollah, S. Amendola, S. N. Morgante, M. G. Deiana, S. Valabrega *et al.*, "Ultrasound sensitivity for thyroid malignancy is increased by real-time elastography: a prospective multicenter study," *The Journal of Clinical Endocrinology & Metabolism*, vol. 97, no. 12, pp. 4524–4530, 2012.

[17] A. E. Samir, M. Dhyani, A. Anvari, J. Prescott, E. F. Halpern, W. C. Faquin, and A. Stephen, "Shear-wave elastography for the preoperative risk stratification of follicular-patterned lesions of the thyroid: diagnostic accuracy and optimal measurement plane," *Radiology*, vol. 277, no. 2, pp. 565–573, 2015.

[18] W. C. Faquin, L. Q. Wong, A. H. Afrogheh, S. Z. Ali, J. A. Bishop, M. Bongiovanni, M. P. Pusztaszeri, C. J. VandenBussche, J. Gourmaud, L. J. Vaickus *et al.*, "Impact of reclassifying noninvasive follicular variant of papillary thyroid carcinoma on the risk of malignancy in the bethesda system for reporting thyroid cytopathology," *Cancer cytopathology*, vol. 124, no. 3, pp. 181–187, 2016.

[19] A. Lorenz, H. Sommerfeld, M. Garcia-Schurmann, S. Philippou, T. Senge, and H. Ermert, "A new system for the acquisition of ultrasonic multicompression strain images of the human prostate in vivo," *ieee transactions on ultrasonics, ferroelectrics, and frequency control*, vol. 46, no. 5, pp. 1147–1154, 1999.

[20] J. Correas, E. Drakonakis, A. Isidori, O. Hélénon, C. Pozza, V. Cantisani, N. Di Leo, F. Maghella, A. Rubini, F. Drudi *et al.*, "Update on ultrasound elastography: miscellanea. prostate, testicle, musculo-skeletal," *European journal of radiology*, vol. 82, no. 11, pp. 1904–1912, 2013.

[21] A. Săftoiu and P. Vilman, "Endoscopic ultrasound elastography-a new imaging technique for the visualization of tissue elasticity distribution," *Journal of Gastrointestinal and Liver Diseases*, vol. 15, no. 2, p. 161, 2006.

[22] T. Selbekk, J. Bang, and G. Unsgaard, "Strain processing of intraoperative ultrasound images of brain tumours: initial results," *Ultrasound in medicine & biology*, vol. 31, no. 1, pp. 45–51, 2005.

[23] T. Selbekk, R. Brekken, O. Solheim, S. Lydersen, T. A. Hernes, and G. Unsgaard, "Tissue motion and strain in the human brain assessed by intraoperative ultrasound in glioma patients," *Ultrasound in medicine & biology*, vol. 36, no. 1, pp. 2–10, 2010.

[24] J. Bercoff, M. Tanter, and M. Fink, "Supersonic shear imaging: a new technique for soft tissue elasticity mapping," *IEEE transactions on*

ultrasonics, ferroelectrics, and frequency control, vol. 51, no. 4, pp. 396–409, 2004.

[25] M. D. Horeh, A. Asif, and H. Rivaz, "Regularized tracking of shear-wave in ultrasound elastography," in *Acoustics, Speech and Signal Processing (ICASSP), 2017 IEEE International Conference on*. IEEE, 2017, pp. 6264–6268.

[26] T. Gallot, S. Catheline, P. Roux, J. Brum, N. Benech, and C. Negreira, "Passive elastography: shear-wave tomography from physiological-noise correlation in soft tissues," *IEEE transactions on ultrasonics, ferroelectrics, and frequency control*, vol. 58, no. 6, pp. 1122–1126, 2011.

[27] K. Nightingale, M. S. Soo, R. Nightingale, and G. Trahey, "Acoustic radiation force impulse imaging: in vivo demonstration of clinical feasibility," *Ultrasound in medicine & biology*, vol. 28, no. 2, pp. 227–235, 2002.

[28] J. Ophir, I. Cespedes, H. Ponnekanti, Y. Yazdi, and X. Li, "Elastography: a quantitative method for imaging the elasticity of biological tissues," *Ultrasonic imaging*, vol. 13, no. 2, pp. 111–134, 1991.

[29] G. Treece, J. Lindop, L. Chen, J. Housden, R. Prager, and A. Gee, "Real-time quasi-static ultrasound elastography," *Interface focus*, vol. 1, no. 4, pp. 540–552, 2011.

[30] C. Schneider, A. Baghani, R. Rohling, and S. Salcudean, "Remote ultrasound palpation for robotic interventions using absolute elastography," in *International Conference on Medical Image Computing and Computer-Assisted Intervention*. Springer, 2012, pp. 42–49.

[31] T. Adebar, S. Salcudean, S. Mahdavi, M. Moradi, C. Nguan, and L. Goldenberg, "A robotic system for intra-operative trans-rectal ultrasound and ultrasound elastography in radical prostatectomy," in *International Conference on Information Processing in Computer-Assisted Interventions*. Springer, 2011, pp. 79–89.

[32] R. Xia, G. Tao, and A. Thittai, "Dynamic frame pairing in real-time freehand elastography," *IEEE transactions on ultrasonics, ferroelectrics, and frequency control*, vol. 61, no. 6, pp. 979–985, 2014.

[33] T. J. Hall, Y. Zhu, and C. S. Spalding, "In vivo real-time freehand palpation imaging," *Ultrasound in medicine & biology*, vol. 29, no. 3, pp. 427–435, 2003.

[34] H. Rivaz, I. Fleming, L. Assumpcao, G. Fichtinger, U. Hamper, M. Choti, G. Hager, and E. Boctor, "Ablation monitoring with elastography: 2d in-vivo and 3d ex-vivo studies," in *International Conference on Medical Image Computing and Computer-Assisted Intervention*. Springer, 2008, pp. 458–466.

[35] G. A. Hendriks, B. Holländer, J. Menssen, A. Milkowski, H. H. Hansen, and C. L. de Korte, "Automated 3d ultrasound elastography of the breast: a phantom validation study," *Physics in Medicine & Biology*, vol. 61, no. 7, p. 2665, 2016.

[36] C. Papadacci, E. A. Bunting, and E. E. Konofagou, "3d quasi-static ultrasound elastography with plane wave in vivo," *IEEE transactions on medical imaging*, vol. 36, no. 2, pp. 357–365, 2017.

[37] A. Bruhn, J. Weickert, and C. Schnörr, "Lucas/kanade meets horn/schunck: Combining local and global optic flow methods," *International journal of computer vision*, vol. 61, no. 3, pp. 211–231, 2005.

[38] T. Varghese, E. Konofagou, J. Ophir, S. Alam, and M. Bilgen, "Direct strain estimation in elastography using spectral cross-correlation," *Ultrasound in medicine & biology*, vol. 26, no. 9, pp. 1525–1537, 2000.

[39] J. Wang, Q. Huang, and X. Zhang, "Ultrasound elastography based on the normalized cross-correlation and the pso algorithm," in *Systems and Informatics (ICSAI), 2017 4th International Conference on*. IEEE, 2017, pp. 1131–1135.

[40] R. Zahiri-Azar and S. E. Salcudean, "Motion estimation in ultrasound images using time domain cross correlation with prior estimates." *IEEE Trans. Biomed. Engineering*, vol. 53, no. 10, pp. 1990–2000, 2006.

[41] L. Yuan and P. C. Pedersen, "Analytical phase-tracking-based strain estimation for ultrasound elasticity," *IEEE transactions on ultrasonics, ferroelectrics, and frequency control*, vol. 62, no. 1, pp. 185–207, 2015.

[42] P. Chaturvedi, M. F. Insana, and T. J. Hall, "Testing the limitations of 2-d companding for strain imaging using phantoms," *IEEE transactions on ultrasonics, ferroelectrics, and frequency control*, vol. 45, no. 4, pp. 1022–1031, 1998.

[43] T. J Hall, P. E Barboneg, A. A Oberai, J. Jiang, J.-F. Dord, S. Goenezen, and T. G Fisher, "Recent results in nonlinear strain and modulus imaging," *Current medical imaging reviews*, vol. 7, no. 4, pp. 313–327, 2011.

[44] C. Pellot-Barakat, F. Frouin, M. F. Insana, and A. Herment, "Ultrasound elastography based on multiscale estimations of regularized displacement fields," *IEEE transactions on medical imaging*, vol. 23, no. 2, pp. 153–163, 2004.

[45] E. Brusseau, J. Kybic, J.-F. Déprez, and O. Basset, "2-d locally regularized tissue strain estimation from radio-frequency ultrasound images: Theoretical developments and results on experimental data," *IEEE Transactions on Medical Imaging*, vol. 27, no. 2, pp. 145–160, 2008.

[46] H. Rivaz, E. Boctor, P. Foroughi, R. Zellars, G. Fichtinger, and G. Hager, "Ultrasound elastography: a dynamic programming approach," *IEEE transactions on medical imaging*, vol. 27, no. 10, pp. 1373–1377, 2008.

[47] A. Kuzmin, A. M. Zakrzewski, B. W. Anthony, and V. Lempitsky, "Multi-frame elastography using a handheld force-controlled ultrasound probe," *IEEE transactions on ultrasonics, ferroelectrics, and frequency control*, vol. 62, no. 8, pp. 1486–1500, 2015.

[48] L. Guo, Y. Xu, Z. Xu, and J. Jiang, "A pde-based regularization algorithm toward reducing speckle tracking noise: A feasibility study for ultrasound breast elastography," *Ultrasonic imaging*, vol. 37, no. 4, pp. 277–293, 2015.

[49] X. Pan, J. Gao, S. Tao, K. Liu, J. Bai, and J. Luo, "A two-step optical flow method for strain estimation in elastography: Simulation and phantom study," *Ultrasonics*, vol. 54, no. 4, pp. 990–996, 2014.

[50] H. Rivaz, E. M. Boctor, M. A. Choti, and G. D. Hager, "Ultrasound elastography using multiple images," *Medical image analysis*, vol. 18, no. 2, pp. 314–329, 2014.

[51] H. Rivaz, E. Boctor, M. Choti, and G. Hager, "Real-time regularized ultrasound elastography," *IEEE transactions on medical imaging*, vol. 30, no. 4, pp. 928–945, 2011.

[52] J. Weickert and C. Schnörr, "A theoretical framework for convex regularizers in pde-based computation of image motion," *International Journal of Computer Vision*, vol. 45, no. 3, pp. 245–264, 2001.

[53] J. Ophir, S. K. Alam, B. Garra, F. Kallel, E. Konofagou, T. Krouskop, and T. Varghese, "Elastography: ultrasonic estimation and imaging of the elastic properties of tissues," *Proceedings of the Institution of Mechanical Engineers, Part H: Journal of Engineering in Medicine*, vol. 213, no. 3, pp. 203–233, 1999.

[54] J. Jensen, "Field: A program for simulating ultrasound systems," *Medical and Biological Engineering and Computing*, vol. 34, pp. 351–352, 01 1996.

[55] Y. Wang, E. Helminen, and J. Jiang, "Building a virtual simulation platform for quasistatic breast ultrasound elastography using open source software: A preliminary investigation," *Medical physics*, vol. 42, no. 9, pp. 5453–5466, 2015.